Research Square

Preprints are preliminary reports that have not undergone peer review.
They should not be considered conclusive, used to inform clinical practice,
or referenced by the media as validated information.

Effect of In-Situ Mechanochemical Activation on the Macroscopic Properties and Microstructure of Graphite Tailings-Based Autoclaved Aerated Concrete

Pei Yang

yangpei@ahiec.edu.cn

Anhui Technical College of Industry and Economy

Kaiqi Sun

Anhui Communications Vocational& Technical College

Article

Keywords: Graphite tailings, Autoclaved aerated concrete, In-situ mechanochemical activation, Compressive strength, Tobermorite

Posted Date: July 3rd, 2026

DOI: https://doi.org/10.21203/rs.3.rs-9982862/v1

License: This work is licensed under a Creative Commons Attribution 4.0 International License.
Read Full License

Additional Declarations: No competing interests reported.

Version of Record: A version of this preprint was published at Scientific Reports on October 16th, 2026. See the published version at https://doi.org/10.1038/s41598-026-75337-y.

Effect of In-Situ Mechanochemical Activation on the Macroscopic Properties and Microstructure of Graphite Tailings-Based Autoclaved Aerated Concrete

Pei Yang[1*], Kaiqi Sun[2]

[1]School of Resources, Environment and Engineering, Anhui Technical College of Industry and Economy, Hefei, Anhui 230051, China

[2]School of Civil and Architectural Engineering, Anhui Communications Vocational& Technical College, Hefei, Anhui 230051, China

*Corresponding Author Email: yangpei@ahiec.edu.cn

Abstract: Graphite tailings (GTs) are hindered from direct AAC application by inherently poor hydrothermal reactivity. This study introduces an alkali-mechanical synergistic, in-situ mechanochemical activation strategy whereby GTs are co-ground with NaOH to boost reactivity for AAC synthesis. Systematic investigation of grinding duration effects reveals that the activation refines pore architecture and concurrently enhances compressive strength while reducing dry density. The 30-min co-ground specimen (A30) delivered optimal properties: 3.89 MPa compressive strength and 626 kg/m³ dry density, fully complying with the A3.5 B06 grade criteria of GB/T 11968–2020. Microstructural analyses verify that the activation accelerates silicon dissolution and intensifies hydrothermal reactions, augmenting tobermorite abundance and crystallinity while fostering a morphological evolution from acicular and fibrous crystals toward plate-like structures. These findings establish a transferable paradigm for GTs valorization and furnish critical theoretical underpinnings for scaling comparable siliceous wastes in sustainable construction materials.

Keywords: Graphite tailings; Autoclaved aerated concrete; In-situ mechanochemical activation; Compressive strength; Tobermorite

1. Introduction

Autoclaved aerated concrete (AAC) offers an attractive combination of lightweight properties, thermal insulation, and fire resistance, making it a widely used wall material in the construction industry [1, 2]. The production and application of AAC align with the principles of sustainable construction, not only effectively reducing carbon emissions and building energy consumption but also generating significant economic and environmental benefits through reduced structural dead load, lower material and labor inputs, and improved indoor thermal comfort and acoustic environments [3, 4]. Conventional AAC production relies primarily on quartz sand, lime, and cement as raw materials, with autoclave curing developing its porous structure [5, 6]. However, natural siliceous raw materials such as quartz sand are non-renewable resources, and their extraction and processing are energy-intensive, posing a critical constraint on the green and sustainable development of the AAC industry. Therefore, utilizing solid wastes to replace natural siliceous raw materials in AAC production

has emerged as an important research direction in this field [7].

Accelerating industrialization and urbanization have intensified solid waste stockpiling and management challenges, establishing resource recovery as a cornerstone of circular economy development [8-10]. Consequently, replacing quartz sand with industrial by-products and agricultural residues in AAC manufacture has attracted growing research interest. Existing literature substantiates the feasibility of employing lithium slag [11], red mud [12], and iron ore tailings [13] as siliceous feedstocks for AAC, attesting to the versatile applicability of waste-derived materials. Nevertheless, the siliceous constituents in these wastes are typically locked in crystalline, chemically inert phases exhibiting poor hydrothermal reactivity, thus requiring activation via physical comminution or chemical pretreatment prior to AAC synthesis. Specifically, Xu et al. [14] achieved A2.5 B05-grade AAC (Chinese standard) by milling copper tailings to 480 m^2/kg specific surface area; Cai et al. [15] demonstrated that enhanced fineness of iron tailings sand improved AAC compressive strength; Wei et al. [16] revealed that NaOH-activated molybdenum tailings undergo accelerated mineral dissolution under hydrothermal conditions, augmenting calcium-silicate-hydrate (C-S-H) precipitation and refining pore structures, with alkali further promoting tobermorite crystallization during autoclaving to collectively boost composite performance.

Graphite tailings (GTs), a typical industrial solid waste generated during graphite mining and beneficiation, hold significant environmental and resource value for utilization. With the expansion of the graphite industry, the cumulative stockpiling of GTs has escalated year by year, drawing increasing attention to the associated land occupation, ecological degradation, and potential water-soil contamination risks [17-19]. Consequently, achieving efficient resource utilization of GTs has become an urgent priority in the resource and environmental sectors. Chemically, GTs are predominantly composed of SiO_2, Al_2O_3, and Fe_2O_3, providing a material basis for their use as siliceous raw materials in AAC [18]. However, similar to most siliceous solid wastes, raw GTs exhibit low hydrothermal reactivity and are unsuitable for direct application in AAC production. Although sole mechanical activation can increase specific surface area and introduce surface defects, its capacity to disrupt crystalline structures at a deeper level remains limited [20]; conversely, sole chemical activation is often constrained by insufficient reaction interfaces, yielding modest improvements in activation efficiency [21]. Therefore, coupling mechanical and chemical activation through an in-situ mechanochemical synergistic approach—wherein chemical activators are introduced simultaneously during the grinding process—holds considerable promise for significantly enhancing the dissolution and transformation efficiency of silicon-aluminum phases in GTs, thereby optimizing the activation outcome. Nevertheless, the underlying synergistic activation mechanism for GTs remains poorly understood, and systematic investigations into how mechanical and chemical activation jointly regulate the hydrothermal product composition, microstructural evolution, and ultimate macroscopic performance of AAC are still lacking.

This study systematically elucidates the enhancement mechanism of hydrothermal reactivity through in-situ mechanochemical synergistic activation by benchmarking against sole mechanical activation, and deciphers the governing principles by which this co-activation

modality regulates AAC product composition and pore architecture. By integrating paste gas evolution behavior and physicomechanical performance testing with comprehensive microstructural characterization via XRD, FTIR, SEM-EDS, and TGA, this work provides mechanistic insights into product formation and microstructural evolution during the hydrothermal processing of GT-based AAC. The findings are expected to offer fundamental insights and practical guidance for the selection and optimization of activation protocols for graphite tailings and analogous siliceous solid wastes, thereby advancing their efficient and high-value utilization in low-carbon building materials.

2. Materials and method

2.1. Raw materials

Raw materials included siliceous materials (graphite tailings and quartz sand), calcareous materials (Portland cement and lime), a chemical activator (sodium hydroxide), gypsum, aluminum powder, and mixing water. The mineralogical phases of GTs and quartz sand are presented in Fig.1. The cement was P·O 42.5 ordinary Portland cement. The sodium hydroxide activator was analytical grade with a purity of ⩾99%. Additionally, aluminum powder with a particle size of 400 mesh was used as the foaming agent. To ensure consistency, all raw materials were sourced from a single batch. The chemical compositions of the primary raw materials were determined by X-ray fluorescence spectrometry (XRF; S8 Tiger, Bruker Scientific Technology Co., Ltd.), with the results summarized in Table 1.

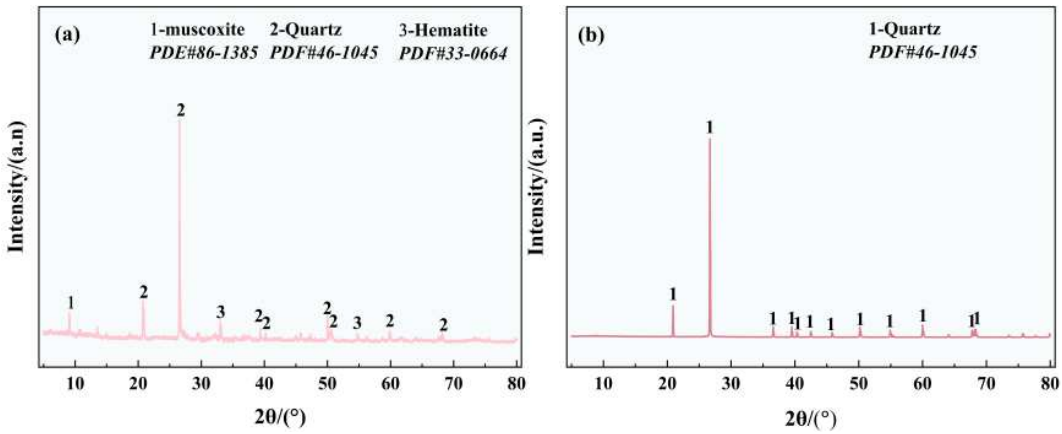

Fig.1. XRD patterns of siliceous materials: (a) GTs, and (b) quartz sand

Table 1

Chemical composition of major raw materials (wt%).

Material	SiO_2	CaO	Al_2O_3	Fe_2O_3	MgO	SO_3	LOI
GTs	60.16	0.62	13.29	7.47	1.82	4.55	12.09
Quartz sand	95.52	1.02	1.32	0.51	0.33	0.31	0.99
Cement	20.13	65.12	4.25	6.12	0.42	1.58	2.38
Lime	1.26	92.16	1.05	0.59	1.24	0.12	3.58
Gypsum	2.34	42.15	0.75	0.23	0.41	49.76	4.36

2.2. GTs pretreatment

Five experimental series were designed to systematically investigate the modification effects of in-situ mechanochemical synergistic activation on GTs, with detailed process parameters

listed in Table 2. A planetary ball mill (QXQM–8, Tencan Powder, China) was employed for the mechanical grinding of GTs at a rotational speed of 300 rpm. Zirconia balls with diameters of 2, 6, 8, and 10 mm were used as grinding media at a number ratio of 10 mm : 8 mm : 6 mm : 2 mm = 1 : 4 : 6 : 2. Each batch was processed in a 2000 mL steel jar charged with 2400 g of zirconia balls, maintaining a ball-to-material mass ratio of 2.4 : 1. Grinding durations were set to 15, 30, and 45 min. The experimental procedure commenced with sole mechanical grinding (15 and 30 min), after which the samples were sealed and stored for subsequent use. Mechanochemical synergistic activation was then performed by externally adding 1 wt% NaOH to the GTs, followed by co-grinding the mixture for 15, 30, and 45 min. All treated GTs samples were collected and hermetically stored for the subsequent AAC preparation.

Table 2

Pretreatment methods of GTs

Sample	Intensive grinding stage (min)	Alkali addition (wt%)
G15	15	0
G30	30	0
A15	15	1
A30	30	1
A45	45	1

2.3. Preparation of AAC

The AAC specimens prepared in this study were designed to conform to the A3.5 B06 grade specified in GB/T 11969–2020 (Test Methods of Autoclaved Aerated Concrete). A water-to-solid ratio of 0.55 was employed. The base mix composition consisted of 35 wt% GTs, 20 wt% quartz sand, 20 wt% cement, 20 wt% lime, and 5 wt% gypsum. Aluminum powder was added at 0.1 wt% of the total dry material mass. The sole experimental variable was the treatment method of GTs (detailed in Table 2), while all other processing parameters were kept constant.

The detailed preparation procedure was as follows. All solid powders were first placed in a high-speed mixer and blended at 200 rpm for 180 s. The rotational speed was maintained, and the predetermined quantity of water was uniformly added within 30 s, followed by continued stirring until a homogeneous slurry was obtained. The slurry was then cast into molds of dimensions 100 mm × 100 mm × 100 mm and 300 mm × 300 mm × 30 mm, and vibrated for 30 s to expel large air bubbles. The molds were subsequently placed in a curing chamber at a constant temperature of 60 °C and allowed to stand for 6 h to facilitate spontaneous expansion and initial hardening. After preliminary hardening, the excess material overflowing from the top of the molds was trimmed, and the specimens were demolded to obtain green bodies of 100 mm × 100 mm × 100 mm and 300 mm × 300 mm × 30 mm. The demolded green bodies were transferred to an autoclave and cured at 190 °C and 1.2 MPa for 10 h to complete the hydrothermal reaction and final hardening. The hardened specimens were then placed in a vacuum drying oven at 40 °C and dried to constant weight for subsequent testing.

2.4. Experimental methods

2.4.1. Fluidity test

The fluidity of the paste was evaluated according to the method described in Ref. [14]. A cylindrical mold with an inner diameter of 50 mm and a height of 100 mm was placed on a smooth glass plate and filled with fresh paste. The mold was then lifted vertically and rapidly. After the paste had flowed to a stable spread, the final diameter was measured along two mutually perpendicular directions, and the average value was taken as the flow spread index.

2.4.2. Gas-foaming evaluation

The foaming process was characterized by monitoring the paste volume as a function of time. One hundred milliliters of paste were poured into a 250 mL graduated cylinder and placed in a curing environment at 50 ± 1 °C. The expansion volume was recorded at 3 min intervals until no further increase was observed (typically lasting 30–60 min). The foaming rate was calculated from the slope of the initial linear stage of the expansion curve.

2.4.3. Bulk density determination

Bulk density was determined in accordance with GB/T 11969-2020 (Test Methods of Autoclaved Aerated Concrete). Three cubic specimens (100 mm × 100 mm × 100 mm) were dried to constant mass in a staged manner at 65 ± 5 °C, 85 ± 5 °C, and 105 ± 5 °C. The dry mass was weighed using an electronic balance, and the specimen dimensions were measured with a digital caliper. The bulk density was then calculated from the dry mass and the measured volume.

2.4.4. Compressive strength test

Compressive strength was determined in accordance with GB/T 11969–2020 (Test Methods of Autoclaved Aerated Concrete). The autoclaved cubic specimens (100 mm × 100 mm × 100 mm) were dried at 60 ± 5 °C to a moisture content of 8–12%. Testing was performed using a microcomputer-controlled electronic universal testing machine (WDW-50E, Jinan Yongbang Instrument Co., Ltd.). Three replicate specimens were tested for each condition, and the average value was reported.

2.4.5. Air pore structure characterization

The surface pore structure of autoclaved specimens was analyzed following the method described in Ref. [22]. High-definition images of the specimen surface (100 mm × 100 mm) were captured using a DJI OSMO Pocket 3 gimbal camera (effective resolution: 12 megapixels). A representative 30 mm × 30 mm region was extracted from the acquired images. The collected cross-sectional images were then subjected to grayscale conversion, median filtering, image enhancement, and binarization, after which quantitative pore information was extracted for statistical analysis.

2.4.6. Thermal conductivity

Thermal conductivity was determined in accordance with GB/T 10294–2008 (Determination of Steady-State Thermal Resistance and Related Properties of Thermal Insulation Materials-Guarded Hot Plate Method). A guarded hot plate apparatus (Model XU8556, Zhengzhou Xiu Instrument Machinery Co., Ltd.) was employed. The specimen dimensions were 300 mm × 300 mm × 30 mm. Prior to testing, specimens were dried at 65 ± 5 °C to

constant mass. Measurements were conducted under steady-state heat flow conditions with a temperature difference of 20 K maintained across the two faces of the specimen.

2.4.7. Microstructural characterization

To characterize the molecular functional groups of the powder specimens after autoclave curing, Fourier transform infrared spectroscopy (FTIR; Nicolet iS5, Thermo Fisher Scientific) was performed using the potassium bromide (KBr) pellet method. Spectra were recorded over a wavenumber range of 500-4000 cm^{-1} at a resolution of 2 cm^{-1}.

Phase composition was analyzed by X-ray diffraction (XRD; D2 PHASER, Bruker AXS) using Cu-Kα radiation (40 kV, 100 mA). The diffraction angle (2θ) was scanned from 5° to 90° at a rate of 5°/min. Phase identification was conducted using JADE 6.5 software with reference to the ICDD PDF-4 database.

Thermogravimetric analysis (TGA; TGA-601, Nanjing Huicheng Instrument Co., Ltd.) was carried out to evaluate the thermal stability and mass evolution of the autoclaved powder specimens. Measurements were performed under a nitrogen atmosphere at a heating rate of 10 °C/min from room temperature to 1000 °C, with both purge and protective gas flow rates maintained at 20 mL/min.

The micro-morphology of hydration products was observed using a scanning electron microscope (SEM; EVO MA 10/LS 10, Carl Zeiss) at an accelerating voltage of 30 kV. The specimens (2.0 mm × 4.0 mm × 5.0 mm) were dried and subsequently sputter-coated with gold to enhance electrical conductivity.

3. Results and discussion

3.1. Fluidity

This section examines the influence of different activation methods on the fluidity of GTs-AAC paste. Paste fluidity is a critical parameter governing the castability of AAC [23]; for A3.5 B06 grade products, the flow spread must typically be maintained within 160–250 mm to ensure proper casting and the development of a desirable pore structure. As shown in Fig.2, the paste fluidity varied significantly depending on the activation protocol. Under sole mechanical grinding, the fluidity of G30 was markedly lower than that of G15. Upon the addition of NaOH for in-situ mechanochemical activation, the fluidity of A15 and A30 was lower than that of their counterparts (G15 and G30) at equivalent grinding durations, and progressively decreased with extended grinding time. The fluidity values followed the descending order: G15 (215 mm) > G30 (204 mm) > A15 (198 mm) > A30 (189 mm) > A45 (175 mm).

The reduction in fluidity observed for G30 relative to G15 is attributed to the increased specific surface area of GTs resulting from prolonged grinding. As reported in previous studies [24], a larger specific surface area promotes the adsorption of free water, thereby reducing the free water content, increasing paste consistency, and consequently lowering the fluidity. The further reduction in fluidity for A15 and A30 arises from the combined ionic and

chemical effects of NaOH. Specifically, NaOH increases the ionic strength of the system, compresses the electric double layer of cement particles, and absorbs free water, thereby diminishing interparticle repulsive forces and inducing flocculation [25], which increases paste consistency. Simultaneously, the high-intensity co-grinding with NaOH partially activates the latent pozzolanic reactivity of GTs, consuming additional free water. Moreover, the highly alkaline environment accelerates cement hydration, fostering the rapid precipitation of hydration products. These synergistic effects collectively increase paste viscosity and reduce fluidity. Additionally, prolonged grinding time during in-situ mechanochemical activation further enhances the pozzolanic reactivity of GTs and enlarges the specific surface area, resulting in a progressive decrease in paste fluidity.

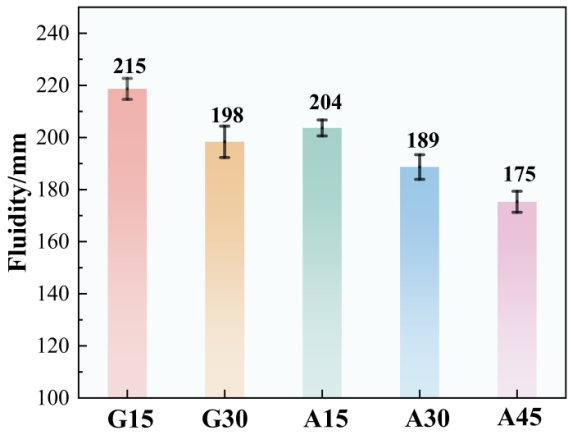

Fig.2. Effect of activation methods on the fluidity of AAC paste.

3.2. Gas–foaming properties aspect

This section investigates the influence of different activation methods on the expansion behavior of GTs-AAC slurry. The expansion rate serves as a critical indicator characterizing the foaming process, directly governing the lightweight characteristics and mechanical performance of AAC. As shown in Fig. 3, the early-stage expansion rate followed the descending order: A45 > A30 > A15 > G30 > G15. The time required to reach the final expansion decreased in the sequence: G15 (39 min) > G30 (33 min) > A15 (27 min) > A30 (24 min) > A45 (18 min), whereas the final expansion rate exhibited the opposite trend: A15 > A30 > G30 > G15 > A45.

The expansion curves of G15 and G30 exhibited four characteristic stages: an induction period, a rapid growth stage, a deceleration stage, and an equilibrium stage. Notably, the in-situ mechanochemically activated specimens (A15, A30, and A45) showed virtually no discernible induction period; the slurry entered the rapid growth stage almost immediately after casting. This indicates that the introduction of NaOH effectively eliminated the induction period. This phenomenon is attributed to the multifaceted role of NaOH: it accelerates the gas evolution rate of aluminum powder [22], promotes flocculation of cement particles by compressing the electric double layer as a strong electrolyte, thereby rapidly increasing the initial viscosity; simultaneously, it activates the latent pozzolanic reactivity of GTs and further accelerates cement hydration, expediting the thickening process. Consequently, by the time the gas evolution reaction commenced, the slurry had already

developed sufficient viscosity to effectively stabilize the initial bubbles, manifesting as a markedly enhanced early-stage expansion rate.

However, the final expansion ratio is governed by the dynamic equilibrium between gas generation and slurry thickening throughout the entire foaming process. For the mechanochemically activated specimens, prolonged grinding time enhanced both the specific surface area and reactivity of GTs, while concurrently accelerating the thickening rate. When the thickening rate became excessively high (as in A45), the slurry viscosity increased rapidly during the early foaming stage. Although this effectively stabilized a large number of initial bubbles, it also prematurely and severely suppressed the subsequent growth, coalescence, and coarsening of bubbles. Thus, despite exhibiting the highest early-stage expansion rate, A45 achieved the shortest final expansion time (18 min) and the lowest final expansion ratio. Conversely, when the thickening rate was better matched with the gas evolution rate (as in A15 and A30), the slurry maintained an appropriately increasing viscosity during the peak gas evolution period. This effectively prevented gas escape without excessively restricting the rational development of bubbles, thereby yielding a higher final expansion ratio.

For the specimens without NaOH (G15 and G30), the final expansion time was substantially prolonged (33 min and 39 min, respectively) compared with the NaOH-containing groups. This is because the slurry failed to develop adequate viscosity during the rapid growth stage, rendering it incapable of effectively retaining gas and resulting in significant gas loss. Consequently, despite exhibiting the longest final expansion times, their low gas utilization efficiency led to unsatisfactory final expansion ratios. In summary, in-situ mechanochemical activation enables the regulation of slurry thickening kinetics; the degree of matching between this thickening behavior and the aluminum powder gas evolution rate determines the final expansion ratio. An optimal activation intensity achieves the best synergy between these two processes, thereby maximizing gas retention efficiency.

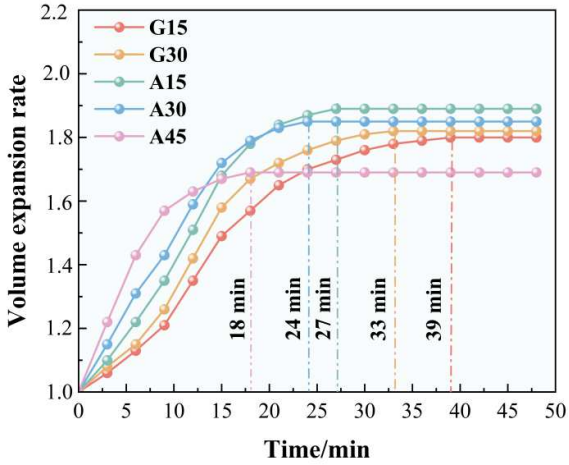

Fig.3. Effect of activation methods on the expansion behavior of AAC slurry.

3.3. Mechanical property and bulk density

This section systematically examines the influence of different activation methods on the compressive strength, dry density, and specific strength of GTs-AAC, elucidating the

pronounced regulatory effect of activation protocol on the mechanical performance and lightweight characteristics of the specimens. Compressive strength and dry density serve as the core performance indicators for AAC. Fig.4a clearly illustrates the divergent effects of the two activation methods on the mechanical properties and dry density of GTs-AAC, while Fig. 4b indicates whether the various specimens meet the requirements for A3.5 B06 grade AAC specified in GB/T 11968-2020.

Under sole mechanical grinding conditions, extending the grinding duration achieved a synergistic optimization of both strength enhancement and density reduction in GTs-AAC. Specifically, the compressive strength of G30 increased by 12.6% compared with G15, while its dry density decreased by 1.7%. This improvement is attributed to the activation effects of mechanical grinding on GTs: the increased specific surface area enlarged the reaction interface with calcium-bearing phases, promoting the formation of hydration products; concurrently, the enhanced specific surface area elevated the slurry viscosity, thereby refining the pore structure, enhancing the gas retention capacity of the slurry, and effectively suppressing bubble coalescence, ultimately leading to the observed performance enhancement.

By contrast, in-situ mechanochemical activation with NaOH yielded superior performance at equivalent grinding times. A15 and A30 outperformed their mechanical-only counterparts (G15 and G30), registering compressive strength gains of 8.3% and 6.0% and dry density reductions of 3.0% and 0.6%, respectively. This improvement derives from NaOH-mediated activation of dormant siliceous phases in GTs [26], which mobilizes additional reactive silica for hydrothermal product formation, coupled with enhanced aluminum powder gas evolution and optimized viscosity development. The improved rheological control effectively stabilizes bubbles, suppressing coalescence, gas loss, and macropore development that would otherwise arise from excessive foaming in low-viscosity slurries.

It is noteworthy that in-situ mechanochemical activation is subject to an optimal intensity threshold. Prolonged grinding (A15→A30→A45) caused compressive strength to peak and subsequently decline, while dry density rose progressively. The A45 formulation exhibited the most severe strength loss and density increase. As evidenced by the rheological and expansion behavior, over-activation drove slurry viscosity beyond the optimal range, arresting expansion and triggering incipient solidification at 18 min. This premature stiffening immobilized bubbles, forcing their coalescence into macropores and interconnected channels rather than facilitating orderly upward migration, thereby catastrophically degrading the pore structure. While over-grinding augmented the reactive silica pool and strengthened hydrothermal reaction intensity, AAC mechanical performance is codetermined by pore architecture and hydration product assemblage [3]. In the A45 regime, the structural penalty imposed by pore deterioration exceeded the reinforcing contribution of enhanced hydration, producing a net decline in mechanical properties.

As shown in Fig.4b, specimens G30, A15, and A30 fully satisfied the requirements for grade A3.5 B06 autoclaved aerated concrete specified in GB/T 11968–2020 with respect to both dry

density and compressive strength. In contrast, although the dry density of G15 met the standard limit, its compressive strength fell below 3.5 MPa, thereby failing to comply with the grade requirements. Conversely, A45 exhibited the opposite trend: while its compressive strength remained within the acceptable range, its dry density exceeded the upper limit prescribed for the A3.5 B06 grade.

Specific strength, serving as a comprehensive indicator for evaluating both the mechanical performance and lightweight characteristics of AAC, further corroborates the aforementioned trends. As shown in Fig.5, specimen G30 exhibited the highest specific strength (6214.1 N·m/kg), whereas A45 displayed the lowest value. This result clearly demonstrates that moderate in-situ mechanochemical activation can synergistically enhance the mechanical performance and lightweight characteristics of GTs-AAC. However, excessive activation induces a mismatch between slurry rheological properties and the gas evolution process, ultimately compromising overall performance.

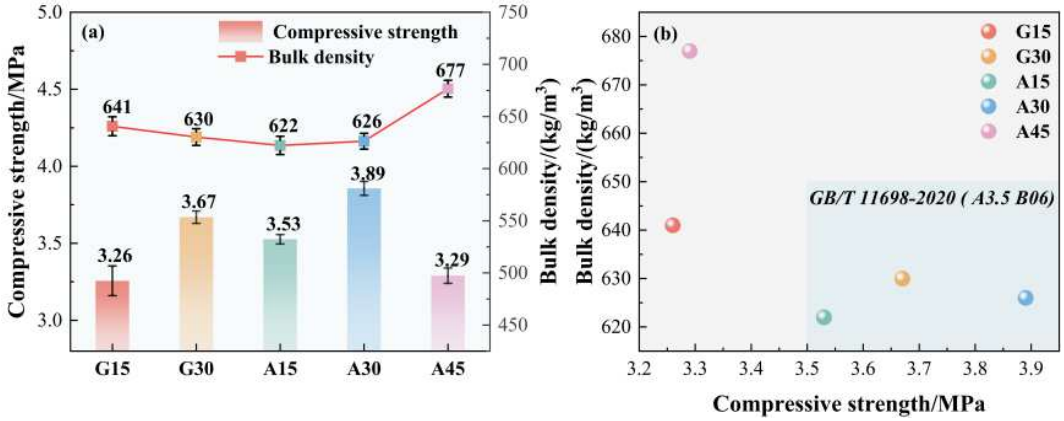

Fig.4. Influence of activation protocol on GTs-AAC performance: (a) compressive strength and dry density; (b) qualification assessment against A3.5 B06 standard.

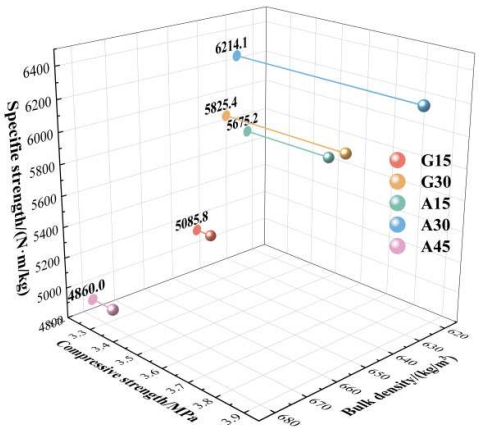

Fig.5. Effect of activation methods on the specific strength of GTs-AAC.

3.4. surface pore structure

To quantitatively characterize the surface pore structure of GTs-AAC, digital image processing was performed on binarized specimen images, enabling a systematic investigation into the regulatory effect of activation method on pore architecture. Fig.6 and Fig.7 present

the surface pore morphology, average pore diameter, and porosity evolution of GTs-AAC under different activation protocols, respectively.

Under sole mechanical grinding conditions, prolonged grinding time significantly improved the pore structure. The average pore diameter of G30 was 1.23 mm, representing a 16.3% reduction compared with G15 (1.47 mm), while the porosity increased from 74.9% to 75.6%. This improvement is primarily attributed to the increased specific surface area of GTs resulting from extended grinding, which enhances slurry viscosity. The appropriately elevated viscosity facilitates bubble stabilization and suppresses bubble coalescence, thereby reducing macropore formation and improving the uniformity of pore distribution. Concurrently, previous studies have indicated that finer particles exert a positive effect on pore formation and stabilization [27], which accounts for the enhanced porosity observed in G30.

The incorporation of NaOH via in-situ mechanochemical activation further refined the pore structure. Notably, specimen A15 exhibited the most favorable pore characteristics, achieving the lowest average pore diameter (0.79 mm) and the highest porosity (79.6%), corresponding to a 46.2% reduction and a 6.3% increase, respectively, relative to G15. Similarly, A30 registered an average pore diameter of 0.84 mm, representing a 31.7% decrease compared with G30, with a concomitant increase in porosity. This enhancement is attributed to the synergistic interplay between NaOH and mechanical grinding: NaOH not only accelerates aluminum powder gas evolution but also collaboratively modulates slurry viscosity with mechanical grinding. This dual action stabilizes bubbles and minimizes gas escape while fostering the formation of a more uniform and refined pore network.

However, excessive mechanochemical activation duration induced severe pore structure degradation. The A45 specimen exhibited an enlarged average pore diameter of 2.13 mm and a diminished porosity of 65.1%, accompanied by the presence of extensive macropores and interconnected voids (Fig. 6e). This deterioration is linked to the mismatch between slurry rheology and gas evolution kinetics: over-grinding caused premature slurry stiffening and excessive viscosity, which impeded bubble migration and promoted bubble coalescence, ultimately yielding a heterogeneous macropore structure. A uniform and fine pore distribution is conducive to alleviating stress concentration and improving mechanical performance, whereas macropores readily serve as stress concentrators that accelerate crack propagation and structural failure [28]. This observation further corroborates the reduction in compressive strength observed for the A45 specimen.

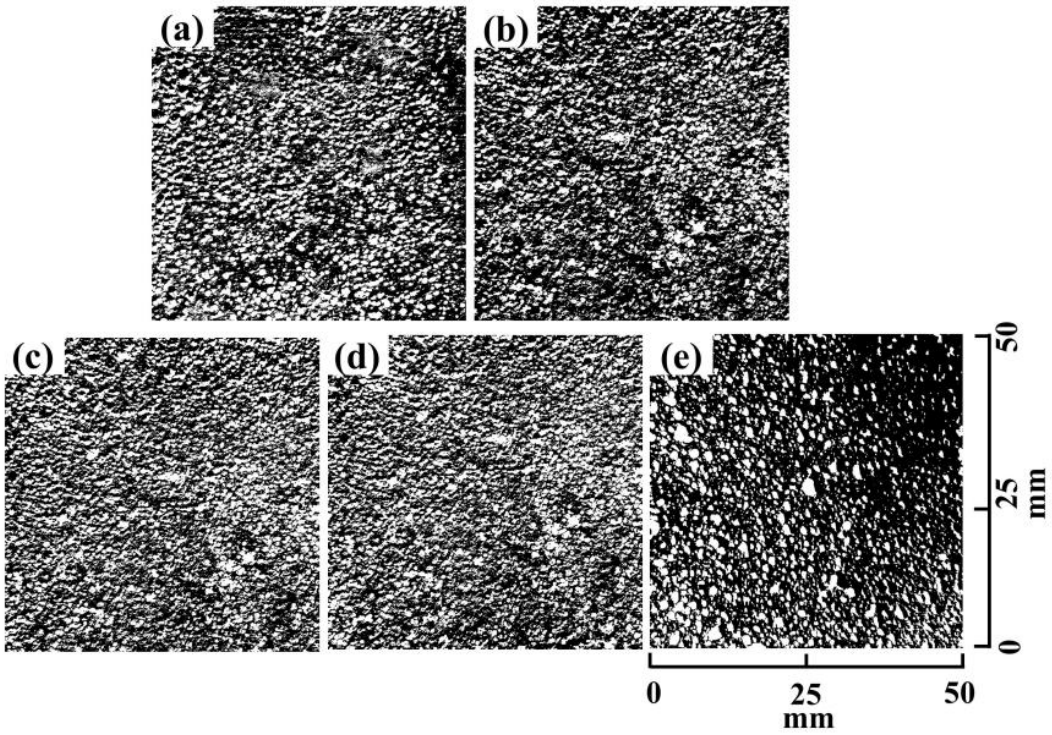

Fig.6. Surface pore morphology of GTs-AAC under different activation methods: (a) G15; (b) G30; (c) A15; (d) A30; (e) A45.

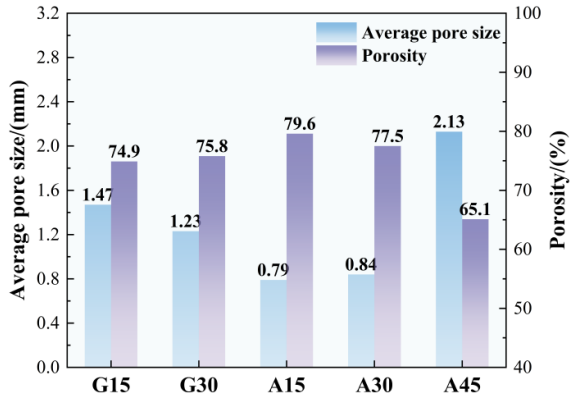

Fig.7. Average pore diameter and porosity of GTs-AAC as a function of activation method.

3.5. Thermal conductivity

Thermal conductivity is a critical indicator for evaluating the thermal insulation performance of AAC. The thermal conductivity values of AAC specimens prepared under different activation methods are presented in Fig.8a. Notably, specimen A15 exhibited the lowest thermal conductivity at 0.143 W/(m·K), whereas A45 displayed the highest value, reaching 0.167 W/(m·K). Except for A45, all other specimens achieved thermal conductivity values below 0.160 W/(m·K), thereby satisfying the thermal performance requirements for grade A3.5 B06 AAC.

Thermal conductivity is primarily governed by the dry density of the material. Generally, higher dry density corresponds to lower porosity and more continuous solid-phase pathways for heat transfer, thereby elevating thermal conductivity. Fig. 8b presents the regression

analysis between thermal conductivity and dry density, revealing a positive correlation (y = 4.49x-0.1343). As discussed in Section 3.3, moderate in-situ mechanochemical activation (e.g., A15) establishes a favorable match between the gas evolution process and slurry rheological properties, fostering a uniform and finely distributed pore structure with high porosity and homogeneous distribution, which consequently yields a lower thermal conductivity. Conversely, excessive activation (e.g., A45) induces premature slurry stiffening, reducing porosity while increasing pore size and promoting the formation of interconnected voids. This facilitates greater heat conduction through the solid skeleton of the pore walls, resulting in a marked increase in thermal conductivity [29].

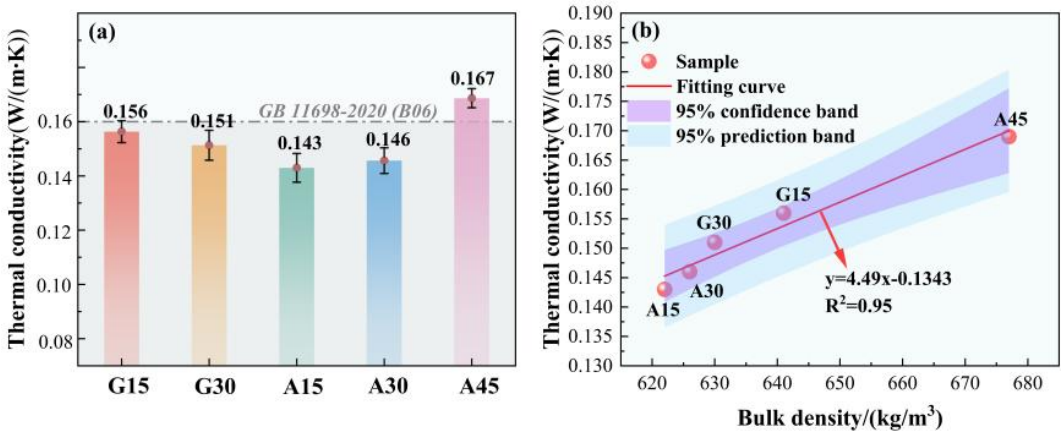

Fig.8. Effect of activation methods on the thermal conductivity of GTs-AAC: (a) thermal conductivity; (b) correlation with dry density.

3.6. Microstructural investigation

3.6.1. X-ray diffraction analysis (XRD)

The mineralogical composition of the hydrothermal products was investigated by X-ray diffraction (XRD) analysis, and the phase contents were quantified using the Rietveld refinement method. Fig. 9 presents the XRD patterns of AAC specimens prepared under different activation methods. Characteristic diffraction peaks corresponding to tobermorite, quartz, calcite, anhydrite, and katoite were detected in all specimens, with peak positions calibrated against ICDD standards.

The XRD patterns (Fig.9) reveal a systematic evolution of tobermorite crystallinity across the activation series. Under sole mechanical grinding, prolonged treatment progressively intensified the tobermorite diffraction peaks, indicating enhanced crystallinity. Mechanistically, mechanical comminution disrupts the inert siliceous framework of GTs, creating fresh surfaces with unsaturated bonds that facilitate silicon dissolution and hydrothermal reaction, thereby promoting tobermorite crystallization. The mechanochemically activated specimens (A15, A30) surpassed their mechanical-only counterparts (G15, G30) in tobermorite peak intensity, reflecting superior crystallinity. This incremental improvement is rooted in the synergistic chemical attack of OH^- on grinding-induced lattice defects [20], which cleaves Si–O–Si bonds and generates highly reactive silicate oligomers that accelerate hydrothermal product formation. Within the mechanochemical series, extending grinding duration from 15 to 45 min (A15→A45)

produced a monotonic yet progressively attenuated increase in tobermorite peak intensity, suggesting a diminishing activation efficiency of NaOH at excessive grinding times.

The persistent quartz reflections originate from unreacted quartz sand and residual crystalline SiO_2 in GTs, functioning as skeletal framework constituents. Anhydrite peaks reflect gypsum dehydration during autoclaving, whereas calcite indicates partial carbonation of hydration products and the inherent carbonate content of GTs. Notably, katoite formation evidences the substitution of Si^{4+} by Al^{3+} within the tobermorite structure under hydrothermal conditions, yielding an Al-substituted tobermorite intermediate that subsequently transforms into katoite [5]. This mineralogical pathway confirms the active participation of Al^{3+} derived from GTs in the hydrothermal reaction network.

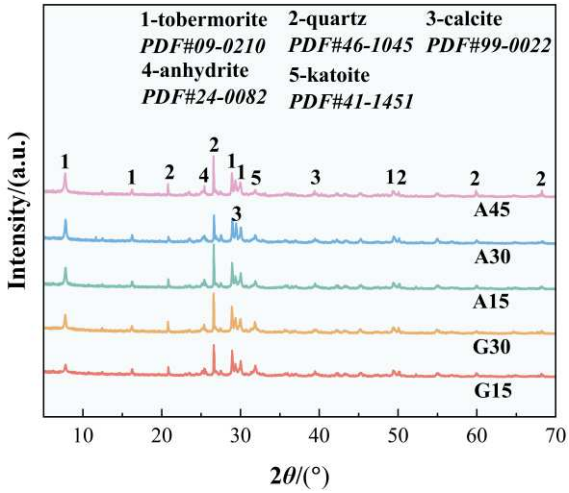

Fig.9. Effect of activation methods on the mineralogical phases of GTs-AAC.

The quantitative phase assemblages derived from Rietveld refinement are shown in Fig.10. Under sole mechanical grinding conditions, the tobermorite content increased from 37.4% in G15 to 41.8% in G30. As the principal hydration product responsible for strength enhancement in AAC [30], this increase in tobermorite content is consistent with the improved compressive strength of G30. Under in-situ mechanochemical activation, the tobermorite content in A15 and A30 specimens further increased, which is attributed to the alkali-mediated promotion of silicon dissolution. This provides a mineralogical explanation for the enhanced macroscopic strength. Notably, although A45 exhibited the highest tobermorite content, the detrimental effect of pore structure degradation outweighed the strength contribution from increased tobermorite formation when grinding time exceeded 30 min, ultimately resulting in the lowest compressive strength.

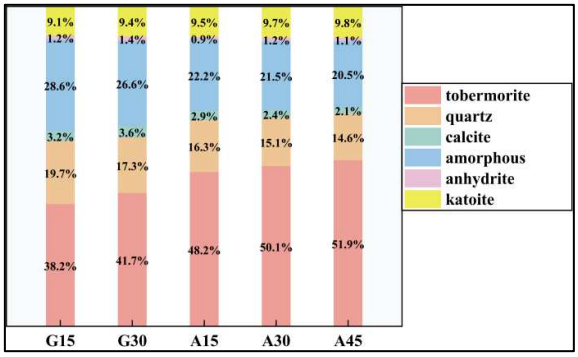

Fig.10. Quantitative phase analysis of GTs-AAC hydrothermal products under different activation methods.

3.6.2. Fourier transform infrared (FTIR)

The characteristic functional groups of the hydrothermal products can be identified from the absorption peaks at specific wavenumbers in the FTIR spectra. Fig.11 presents the FTIR spectra of AAC specimens prepared with GTs subjected to different activation methods. The high-frequency region between 4000 and 2000 cm^{-1}, which is dominated by O–H stretching vibrations, is not shown here as it is beyond the scope of this study [5]. The spectral profiles of all specimens were similar, indicating that the different activation methods did not introduce new chemical bonds or functional groups; rather, they only induced variations in peak position and intensity.

The absorption band near 1640 cm^{-1} is attributed to the H-O-H bending vibration of adsorbed water [31], originating primarily from weakly bound water physically adsorbed within gel pores or on the surfaces of hydration products. The absorption peak near 1420 cm^{-1} corresponds to the asymmetric stretching vibration of C-O bonds [32], consistent with the calcite phase identified by XRD. The peak at 960 cm^{-1} represents the asymmetric stretching vibration of Si-O-Si bonds within the silicate network [33], indicating the formation of C-S-H gel in the system. The absorption band at 671 cm^{-1} is assigned to the bending vibration of Si-O-Si bonds, confirming the presence of tobermorite [34]. Notably, the Si–O–Si bending vibration peak shifted slightly from 670 to 673 cm^{-1}, a shift typically associated with an increased degree of polymerization of the silicate network [35]. This indicates that in-situ mechanochemical activation promotes the dissolution of siliceous phases in GTs, thereby driving the development of the tobermorite structure toward a higher degree of polymerization during hydrothermal processing.

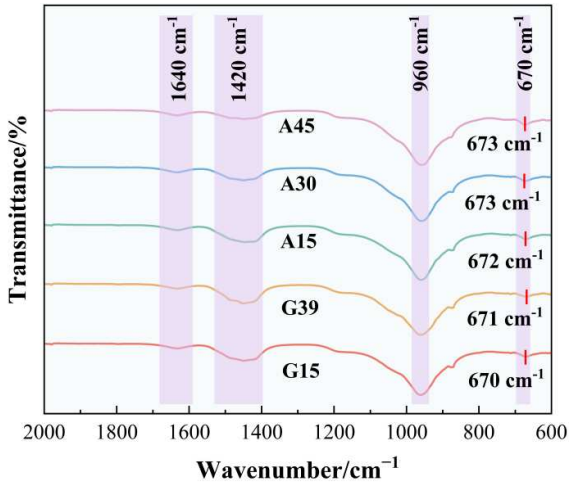

Fig. 11. FTIR spectra of GTs-AAC specimens prepared under different activation methods.

3.6.3. Thermal analysis

Thermogravimetric analysis (TGA) was employed to characterize the AAC specimens prepared under different activation methods, in order to investigate their dehydration, decarbonation, and decomposition behavior of hydration products during heating. As shown in Fig.12, the mass loss curves of all specimens exhibited three distinct weight loss stages.

The first stage (room temperature to 320 °C) corresponds primarily to the removal of physically adsorbed water from the gel products [23]. The pronounced fluctuations in the DTG curves within this interval indicate significant dehydration reactions. The mass loss for the various specimens followed the descending order: G15 (6.64%) > G30 (6.55%) > A30 (6.26%) > A15 (6.21%). These results demonstrate that both mechanical grinding and mechanochemical activation promote the formation of hydration products, with the latter exhibiting a more pronounced effect, consistent with the quantitative XRD analysis.

The second stage (320-600 °C) is attributed to the release of bound water from tobermorite [21]. The DTG curves in this region exhibited relatively moderate fluctuations. The mass loss decreased in the order: G15 (2.91%) > G30 (2.48%) > A30 (2.44%) > A15 (2.39%). This indicates that mechanochemical activation further increases tobermorite yield, and that the reactivity of graphite tailings is progressively enhanced with extended activation time, thereby promoting the hydrothermal reaction and elevating the tobermorite content—a finding that corroborates the XRD phase quantification results.

The third stage (600-800 °C) is mainly associated with the decomposition of calcite [36]. The mass loss followed the sequence: A15 (2.50%) > A30 (2.45%) > G30 (2.41%) > G15 (2.06%). This suggests that the elevated alkalinity of the system favors the conversion of $Ca(OH)_2$ into C-S-H, thereby reducing the relative calcite content.

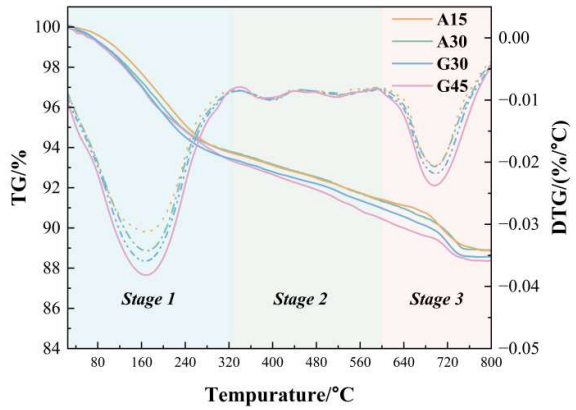

Fig.12. TG-DTG curves of GTs-AAC specimens prepared under different activation methods.

3.6.4. SEM analysis

Fig.13 presents the microstructures of AAC specimens prepared with GTs subjected to different activation methods. All specimens exhibited well-developed crystalline structures, with crystals interconnecting and interlacing to form a continuous network framework, thereby producing a relatively dense micro-morphology. However, distinct morphological characteristics of the hydration products were observed among the different specimens, indicating that the activation method significantly influenced their formation process, particularly with respect to the morphology and distribution of tobermorite.

Combined with EDS analysis and literature results [37], the specimens subjected to sole mechanical grinding primarily exhibited needle-like tobermorite in G15 (Fig. 13a) and grass-like tobermorite in G30 (Fig. 13b). This morphological difference is attributed to the

enhanced reactivity of siliceous constituents resulting from prolonged grinding time, which subsequently influenced crystal growth. Previous studies have indicated that needle-like tobermorite exerts a detrimental effect on mechanical properties [37], a finding consistent with the compressive strength results obtained in this study.

By contrast, specimens A15 and A30 subjected to in-situ mechanochemical activation (Fig.13c and d) predominantly exhibited plate-like tobermorite morphologies. This morphological transition is closely associated with the NaOH-promoted dissolution of GTs and the consequent nucleation and growth of tobermorite. Plate-like tobermorite has been widely demonstrated to enhance AAC strength more effectively than needle-like or fibrous morphologies [38], which provides a microstructural rationale for the superior compressive strength observed in the mechanochemically activated specimens.

A comparative analysis of specimens A15, A30, and A45—all subjected to the same mechanochemical activation protocol but with varying grinding durations—revealed that, although plate-like tobermorite predominated in all three formulations, significant differences were evident in crystal dimensions, distribution density, and crystallographic perfection. The crystals in A15 were predominantly slender and elongated, whereas those in A30 and A45 developed into coarser, blocky morphologies with progressively increasing yield as grinding time was extended, consistent with the XRD and TG analyses. This microstructural evolution explains the lower compressive strength of A15 relative to A30.

Notably, despite A45 exhibiting the highest tobermorite content and crystallinity among all specimens, its macroscopic compressive strength was the lowest. This is primarily attributed to the fact that the ultimate mechanical performance of AAC is governed by the synergistic interplay between hydration products and pore architecture. As illustrated in Fig. 6e (Section 3.4), the A45 specimen exhibited a marked proliferation of macropores. The detrimental effect of pore structure degradation offset the positive contribution of enhanced hydration product formation, thereby resulting in strength reduction.

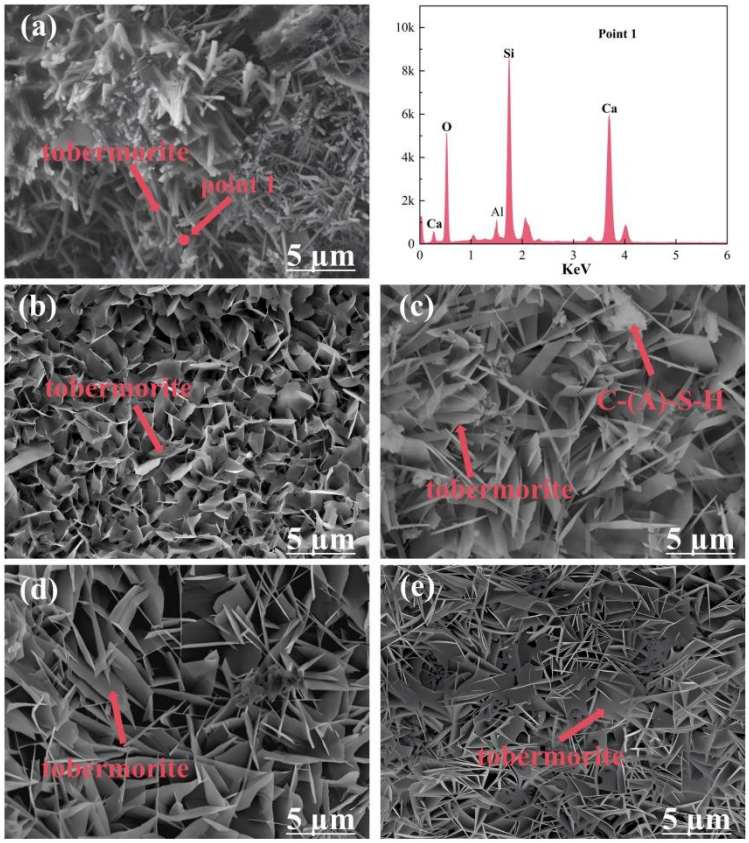

Fig.13. SEM micrographs of GTs-AAC hydrothermal products under different activation methods: (a) G15; (b) G30; (c) A15; (d) A30; (e) A45.

4. Conclusion

This study confirms the feasibility of employing in-situ mechanochemical activation as a pretreatment strategy for utilizing graphite tailings (GTs) in autoclaved aerated concrete (AAC) production. The proposed activation method significantly enhanced the macroscopic performance and microstructural characteristics of GTs-AAC, achieving a favorable balance among compressive strength, dry density, and thermal conductivity. This work establishes a novel pathway for the high-value resource utilization of analogous siliceous solid wastes. The principal conclusions are as follows:

(1) In-situ mechanochemical activation enables synergistic modulation of slurry rheological properties and gas evolution kinetics, enhancing pore structure stability and thereby improving the mechanical performance of AAC. Among all formulations, specimen A30 achieved the optimal compromise among compressive strength (3.89 MPa), dry density (626 kg/m³), and thermal conductivity (0.146 W/(m·K)), fully satisfying the requirements for grade A3.5 B06 AAC specified in GB/T 11968–2020. However, excessive grinding leads to excessively high slurry viscosity, pore coarsening, and elevated porosity, which conversely induce strength deterioration and increased thermal conductivity.

(2) Sole mechanical grinding disrupts the crystalline structure of GTs, increasing the specific surface area and reactive sites, which promotes the dissolution of SiO_2 during hydrothermal processing and thereby accelerates tobermorite crystallization and formation. Building upon this, the introduction of NaOH in in-situ mechanochemical activation further stimulates the latent pozzolanic reactivity of GTs and significantly enhances the formation and

transformation of C-S-H gel, resulting in a further increase in tobermorite content and more complete crystallization.

(3) In-situ mechanochemical activation exerts a critical modulating effect on the crystal morphology of tobermorite. Compared with the needle-like and fibrous tobermorite formed under sole mechanical grinding, this activation method promotes the development of plate-like crystal morphologies that are more favorable for mechanical performance. This is primarily attributed to the alkali-accelerated dissolution and reorganization of silico-aluminous constituents, which optimizes the reaction pathway and nucleation environment for hydrothermal synthesis.

In summary, an optimal grinding duration is critical for enhancing the performance of GTs-AAC. This study provides theoretical insights and technical guidance for the practical application of in-situ mechanochemical activation in AAC production. Future work may focus on further optimizing the activator dosage and processing parameters to improve material performance while advancing the green and low-carbon development of building materials.

Data Availability Statement

The datasets used and/or analysed during the current study are available from the corresponding author on reasonable request.

Funding

This research was funded by the Scientific Research Project of Higher Education Institutions in Anhui Province, Anhui Provincial Department of Education (Grant No. 2024AH050181), and the Provincial Quality Engineering Project of Higher Education Institutions in Anhui Province (Grant No. 2023jnds040).

References

[1] Pihelo P, Kalamees T. Performance evaluation and development of prefabricated insulation elements for renovation of apartment buildings with autoclaved aerated concrete external walls. Energy and Buildings. 2025;332.

[2] Michelini E, Ferretti D, Miccoli L, et al. Autoclaved aerated concrete masonry for energy efficient buildings: State of the art and future developments. Construction and Building Materials. 2023;402.

[3] Xu R, Kong F, Tong H, et al. Performance enhancement of copper tailings-based autoclaved aerated concrete through chemical activation: From macro-properties to microstructure evolution. Construction and Building Materials. 2025;500.

[4] Ricciotti L, Occhicone A, Petrillo A, et al. Geopolymer-based hybrid foams: Lightweight materials from a sustainable production process. Journal of Cleaner Production. 2020;250.

[5] Gu XW, Wang SY, Liu JP, et al. Comparative analysis of coal-derived and biomass-derived fly ash as silica sources in autoclaved aerated concrete. Construction and Building Materials. 2025;491.

[6] Jiang J, Lu XL, Niu T, et al. Performance optimization and hydration characteristics of BOF slag-based autoclaved aerated concrete (AAC). Cement & Concrete Composites.

2022;134.
[7] Dauksza P. Autoclaved Aerated Concrete AAC in sustainable construction. Cement Wapno Beton. 2022;27:224-40.
[8] Luo S, Li S, Wang Y, et al. Mechanism of hydration and structure formation of autoclaved aerated concrete with multiple solid wastes. Construction and Building Materials. 2025;467.
[9] Nwachukwu MA, Ronald M, Feng H. Global capacity, potentials and trends of solid waste research and management. Waste Management & Research. 2017;35:923-34.
[10] Gu JR, Liu XM, Zhang ZQ. Road base materials prepared by multi-industrial solid wastes in China: A review. Construction and Building Materials. 2023;373.
[11] Wang SY, Gu XW, Liu JP, et al. Assessment of lithium slag as a supplementary siliceous material in autoclaved aerated concrete: Physical properties and hydration characteristics. Construction and Building Materials. 2024;442.
[12] Song YF, Dong MH, Wang ZG, et al. Effects of red mud on workability and mechanical properties of autoclaved aerated concrete (AAC). Journal of Building Engineering. 2022;61.
[13] Liang XY, Yuan DX, Li J, et al. PREPARATION AND PHASE CHARACTERISTICS OF AUTOCLAVED AERATED CONCRETE USING IRON ORE TAILINGS. Revista Romana De Materiale-Romanian Journal of Materials. 2018;48:381-7.
[14] Xu R, Tong H, Kong F, et al. Potential of copper tailings as supplementary siliceous materials in the preparation of autoclaved aerated concrete. Journal of Building Engineering. 2024;98.
[15] Cai LX, Ma BG, Li XG, et al. Mechanical and hydration characteristics of autoclaved aerated concrete (AAC) containing iron-tailings: Effect of content and fineness. Construction and Building Materials. 2016;128:361-72.
[16] Wei J, Yu XY, Gao W, et al. High-performance autoclaved aerated concrete fabricated by alkali-activated low-silica molybdenum tailings. Construction and Building Materials. 2025;484.
[17] Kathirvel P, Kwon SJ, Lee HS, et al. Graphite Ore Tailings as Partial Replacement of Sand in Concrete. Aci Materials Journal. 2018;115:481-92.
[18] Peng YZ, Liu YJ, Zhan BH, et al. Preparation of autoclaved aerated concrete by using graphite tailings as an alternative silica source. Construction and Building Materials. 2021;267.
[19] Zhang JL, Wei Q, Zhang N, et al. Comparative Study of Iron-Tailings-Based Cementitious Mortars with Incorporated Graphite Ore and Graphite Tailings: Strength Properties and Microstructure. Materials. 2023;16.
[20] Li PY, Ren ZJ, Xie EJ, et al. Application of mixed collectors on quartz-feldspar by fluorine-free flotation separation and their interaction mechanism: A review. Physicochemical Problems of Mineral Processing. 2021;57:139-56.
[21] Xu RS, Kong FH, Tong H, et al. Performance enhancement of copper tailings-based autoclaved aerated concrete through chemical activation: From macro-properties to microstructure evolution. Construction and Building Materials. 2025;500.
[22] Xu XC, Wang SY, Gu XW, et al. Intensive grinding assisted alkali modification of iron tailings sands for aerated concrete preparation: Dual contribution to hydrothermal product and pore stability. Construction and Building Materials. 2025;504.
[23] Wei C, Wu PF, Gu JR, et al. Potential of titanium gypsum in autoclaved aerated concrete

for large incorporation: Hydration characteristics and performance optimization. Construction and Building Materials. 2025;473.
[24] Huang W, Quan WL, Bu XZ, et al. Preparing autoclaved aerated concrete using high-silicon iron tailing. Construction and Building Materials. 2023;408.
[25] Huang TJ, Zhang K, Kang KG, et al. The effect of NaOH addition on the physico-chemical phenomena of cement setting acceleration. Construction and Building Materials. 2025;458.
[26] Li ZJ, Gu XW, Yang BH, et al. Optimizing the utilization of bauxite tailings in low-carbon cement. Construction and Building Materials. 2025;462.
[27] Xiao JZ, Lv ZY, Duan ZH, et al. Pore structure characteristics, modulation and its effect on concrete properties: A review. Construction and Building Materials. 2023;397.
[28] Gu X, Wang S, Liu J, et al. Effect of hydroxypropyl methyl cellulose (HPMC) as foam stabilizer on the workability and pore structure of iron tailings sand autoclaved aerated concrete. Construction and Building Materials. 2023;376.
[29] Liu P, Luo A, Liu L, et al. Study on the preparation and performances analysis of lightweight high strength ceramsite aerated concrete. Journal of Materials Research and Technology-Jmr&T. 2023;25:6672-83.
[30] Dong MH, Ruan SQ, Zhan SL, et al. Utilization of red mud with high radiation for preparation of autoclaved aerated concrete (AAC): Performances and microstructural analysis. Journal of Cleaner Production. 2022;347.
[31] Lothenbach B, Jansen D, Yan Y, et al. Solubility and characterization of synthesized 11 Å Al-tobermorite. Cement and Concrete Research. 2022;159.
[32] Luo SQ, Li SH, Wang YL, et al. Mechanism of hydration and structure formation of autoclaved aerated concrete with multiple solid wastes. Construction and Building Materials. 2025;467.
[33] Chen X, Guo YH, Gong TT, et al. Study on preparation and performance of brick-concrete recycled sand powder autoclaved aerated concrete. Journal of Building Engineering. 2024;91.
[34] Liu KW, Shen CZ, Wang YM, et al. The performance of autoclaved aerated concrete prepared by arenaceous rock coal gangue powder instead of fly ash: The effect of Ca/Si ratio. Construction and Building Materials. 2024;441.
[35] Zhong DQ, Wei SH, Zhou H, et al. The Influence of Retreated Lithium Slag with a High Content of Alkali, Sulfate and Fluoride on the Composition and the Microstructure of Autoclaved Aerated Concrete. Materials. 2024;17.
[36] Wu RD, Dai SB, Jian SW, et al. Utilization of solid waste high-volume calcium coal gangue in autoclaved aerated concrete: Physico-mechanical properties, hydration products and economic costs. Journal of Cleaner Production. 2021;278.
[37] Jiang J, Ma B, Cai Q, et al. Utilization of ZSM-5 waste for the preparation of autoclaved aerated concrete (AAC): Mechanical properties and reaction products. Construction and Building Materials. 2021;297.
[38] Peng Y, Liu Y, Zhan B, et al. Preparation of autoclaved aerated concrete by using graphite tailings as an alternative silica source. Construction and Building Materials. 2021;267.